Laser Powder Bed Fusion printability of cobalt-free steel powders for manufacturing injection molds

Quentin Saby, Jean-Yves Buffière, Eric Maire, Thomas Joffre, Julien Bajolet, Stéphane Garabédian, Peter Vikner, Xavier Boulnat

Graphical Abstract

Laser Powder Bed Fusion printability of cobalt-free steel powders for manufacturing injection molds

Quentin Saby, Jean-Yves Buffière, Eric Maire, Thomas Joffre, Julien Bajolet, Stéphane Garabédian, Peter Vikner, Xavier Boulnat

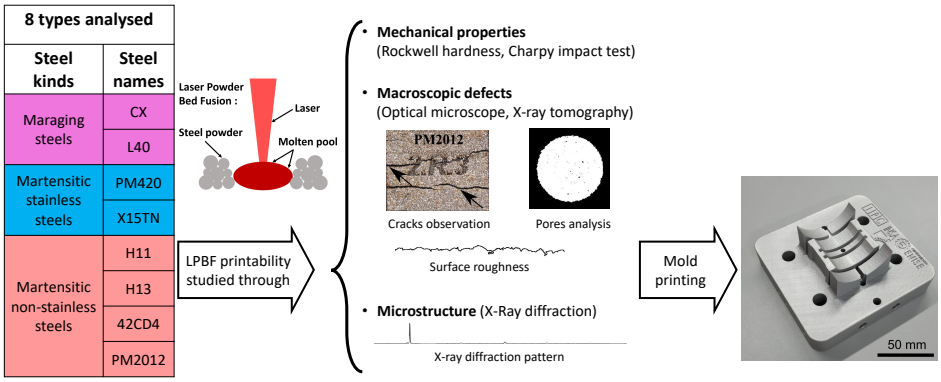

Laser Powder Bed Fusion printability of cobalt-free steel powders for manufacturing injection molds

Quentin Saby[a,b,*], Jean-Yves Buffière[a], Eric Maire[a], Thomas Joffre[b], Julien Bajolet[b], Stéphane Garabédian[b], Peter Vikner[c], Xavier Boulnat[a]

[a] *Université de Lyon, INSA Lyon, MATEIS UMR CNRS 5510, F69621 Villeurbanne, France*
[b] *Centre Technique Industriel de la Plasturgie et des Composites, Bellignat, France*
[c] *Aubert & Duval, Paris, France*

Abstract

Laser Powder Bed Fusion (LPBF) printing is used for manufacturing conformal cooling injection molds with internal cooling channels. Currently, the steel used to manufacture such molds by LPBF is the maraging 18Ni300. However, this steel is softer at high temperatures and less resistant to corrosion than the reference steel, the AISI H11. Moreover, 18Ni300 contains cobalt, an element that can be harmful to the health of people handling powders made of this steel. In order to find a cobalt-free alternative to 18Ni300, the printability of three different types of steel is studied: maraging stainless steels (CX, L40), martensitic non-stainless steels (42CD4, H11, H13, PM2012) and martensitic stainless steels (X15TN, PM420). The printability of those eight steels is studied through their mechanical properties (Rockwell hardness, Charpy impact test), their internal defects and surface roughness (X-ray tomography), the presence of cracks (optical microscope), and also through their microstructure (X-ray diffraction) in the as-built state. The results show that the stainless steels (PM420, X15TN, L40 and CX) exhibit interesting as-built properties allowing them to be considered as a possible alternative to the maraging steel 18Ni300 to produce LPBFed injection molds. A conformal cooling injection mold was then printed as a demonstrator.

Keywords: Laser Powder Bed Fusion, Conformal Cooling, Martensitic Steels, Mechanical Properties, X-ray Tomography

1. Introduction

The development of Additive Manufacturing technologies (AM), which has accelerated sharply in recent years, offers the possibility of designing parts and sets of parts that were previously impossible to achieve with traditional manufacturing processes such as milling, drilling or turning. In the case of traditional machining, parts are made by removing material, whereas in AM, parts are made by successive additions of layers of material and this allows new design possibilities, such as parts containing lattice structures or containing internal cooling channels [1][2][3].

Metallurgical issues encountered during welding can also be found in LPBF printing since this method consists of creating weld beds horizontally and then superimposing them vertically. Therefore, the most commonly used steels are those whose good weldability is known, mainly low-carbon steels such as 18Ni300 or 316L steels [4][5][6][7][8][9].

In the plastic industry, LPBF printing enables the design of injection molds with internal 'conformal cooling' channels that fit the mold shape as closely as possible and ensure homogeneous and quick cooling of the part before it is ejected from the mold thus increasing the cost and energy efficiency of the process (see Figure 1) [10][11].

*Corresponding author

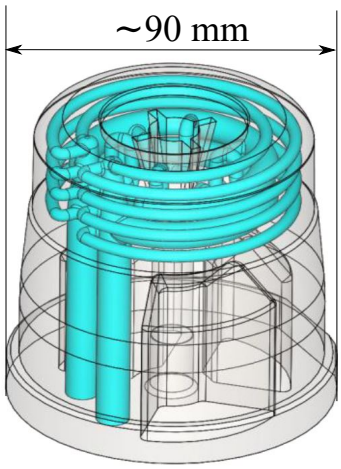

Figure 1: Mold printable by LPFB with conformal cooling channels as close as possible to the molding shape to ensure quick and homogeneous cooling of the injected part (courtesy of IPC and Smoby)

AISI H11 and AISI H13 tool steels are the reference alloys for manufacturing respectively plastic injection molds and die casting molds by traditional machining. Tool steels have a carbon content between 0.3 and 0.6 wt.%, which confers high hardness and low ductility after quenching, making them difficult to weld and therefore to print. The compressive and tensile stresses which appear during the heating and cooling cycles of printing cause the most brittle zones to break in tool steels [11][12]. A tempering or double tempering heat treatment is necessary to lower the hardness and improve the ductility. For the reasons stated above, tool steels are difficult to print with LPBF. Therefore, numerous studies have been carried out on the printing of molds from such steels [13][14][15][16][17]. However neither H11 nor H13 large-scale molds printed by LPFB have been found in literature yet.

So far the strategy for printing injection molds has been to use maraging steels whose good printability is known. Printability is the ability of a steel to form parts without cracks, and with the fewest defects (pores, roughness) which could be areas of stress concentration and lead to a degradation of the mechanical properties. Low-carbon maraging steels exhibit good printability thanks to a soft martensitic structure that is further hardened by precipitation hardening. A good example of such steel is the 18Ni300 alloy, its high nickel content (about 18 wt.%) allows the formation of martensite by cooling in ambient air. The hardening of 18Ni300 is mainly due to the formation of Ni_3Ti precipitates created during an ageing treatment, it is accompanied with a decrease in ductility [18]. The major drawbacks of 18Ni300 is that its hardness is lower than that of tool steels at high temperatures, its price is high due to its high-nickel content [10] and its corrosion resistance is low due to the absence of chromium in its composition.

For all these reasons, in spite of their potential, none of those steels (tool steels and maraging steels) fulfills perfectly the manifold requirements for producing an injection mold by LPFB. The topic of this study is therefore to extend the search for good printability, by studying several kinds of steels: maraging stainless steels, martensitic non-stainless steels (traditional tool steels), and martensitic stainless steels.

As cobalt has detrimental health impact and as it is a rare and expansive alloying element, all steels analysed in this study are cobalt-free [19][20].

In this work, printability is assessed by examining the mechanical properties (Rockwell hardness, Charpy impact test), defects and roughness (X-ray tomography, optical microscopy), and also through their microstructure (X-ray diffraction) in the as-built state.

2. Experimental

2.1. Atomised Powders

X15TN, PM420, PM2012 and 42CD4 powders were provided by Aubert & Duval; L40 powder was provided by Nanosteel; H11 and H13 powders were provided by LPW; CX powder was provided by EOS.

All powders had a particle size between 20 and 53 μm and were gas atomised. Chemical compositions of the steels used are given in Table 1 and were found in the technical documentation of the suppliers, except for L40 whose composition was found in the patent [21] and for PM420 whose composition was provided by Aubert & Duval.

Table 1: Chemical compositions of the steels in wt.% based on the supplier documentation

Steel types	Steel names		C	Mn	Cr	Mo	V	Ni	Cu	Si	Al	Ti	W	N	Fe
Martensitic stainless steels	**PM420 (X30Cr13 - AISI 420)**		0.35	0.28	13.7	0.028		0.109	0.014	0.36		0.003	0.03		//
	X15TN (X40CrMoVN16-2)	Min	0.37	-	15.00	1.50	0.20	-		-				0.16	//
		Max	0.45	0.60	16.50	1.90	0.40	0.30		0.60				0.25	
Martensitic steels	**42CD4 (42CrMo4)**	Min	0.38	0.6	0.9	0.15				-					//
		Max	0.45	0.9	1.2	0.3				0.4					
	AISI H11 (X37CrMoV5-1)	Min	0.35	0.20	4.75	1.10	0.30			0.80					//
		Max	0.45	0.60	5.50	1.60	0.60			1.25					
	AISI H13 (X40CrMoV5-1)	Min	0.32	0.20	4.75	1.10	0.80	-	-	0.80				-	//
		Max	0.45	0.50	5.50	1.75	1.20	0.30	0.25	1.20				0.1	
	PM2012 (HS 2-2-2)		0.6	0.3	4.0	2.0	1.5			1.0			2.1		//
Maraging stainless steels	**L40**		0.16		10.64	1.48		1.96	0.54	0.19				0.07	//
	CX	Min	-	-	11.00	1.10		8.40		-	1.20				//
		Max	0.05	0.40	13.00	1.70		10.00		0.40	2.00				

2.2. Laser powder bed fusion

The samples were printed with an EOS INT M270 machine. The melting parameters used are listed in Table 2. To compare the printability of the different steels with respect to their chemical composition, average melting parameters were used with two different energy densities. Previous internal experiments, had shown that stainless steels require higher energy density than the one used to print non-stainless steels, respectively 93±11 J/mm^3 and 60±7 J/mm^3 [22][23]. Consequently two sets of parameters have been used : one set for PM2012, 18Ni300, 42CD4, H11 and H13 steels on the hand, and another set for the PM420, L40, CX and X15TN stainless steels on the other hand (Table 2). The laser power and the hatch distance were set at 195 W and 100 μm respectively, the layer thickness was 40 μm for the steels and 30 μm for the stainless steels. A layer thickness of 40 μm was chosen for martensitic non-stainless steels to reduce residual stresses during printing. Studies have shown that increasing the layer thickness can reduce residual stresses by reducing the thermal gradient in the printed layer [24][25][26]. The orientation of hatching was 67° per layer. The scan speed v_s (mm/s) was determined using the formula

$$v_s = \frac{P}{E_d \times h \times d}$$

where E_d is the energy density (J/mm^3), P is the laser power (W), h is the hatch distance (mm) and d is the layer thickness of the powder bed (mm).

Table 2: Melting parameters : two different sets of parameters were used to print the stainless steels and the non-stainless steels

	Non-stainless steels	**Stainless steels**
P - Laser power [W]	195	195
v_s - Scan speed [mm.s^{-1}]	818	699
d - Layer thickness [μm]	40	30
h - Hatch distance [μm]	100	100
E_d - Energy density[J/mm^3]	60	93

2.3. Mechanical properties characterization

Hardness measurements were performed with a Wolpert R-Testor 643R. Before indentation, the specimen surfaces were polished with P320 sandpapers to remove the initial roughness.

Charpy impact tests were carried out with a Zwick Roell Charpy impact test machine. The Charpy specimen dimensions were 5 × 10× 55 mm^3 and had 5 mm U-shaped notches, in accordance with the NF EN ISO 148-1 (2017) standard. The external surfaces were milled and the notches were made by Electrical Discharge Machining (EDM).

2.4. Defects characterization

Optical observations were carried out using a Hirox RH-2000 optical microscope. SEM observations were made with a Zeiss SUPRA 55 field emission gun microscope.

X-ray tomography was performed with a v|tome|x s tomograph made by General Electric TM, using a voxel size of 3 μm. A voltage of 140 kV and an intensity of 80 μA were used to scan cylindrical samples with a 3 mm diameter and 10 mm length. 1200 projections were made per scan and the scan time was approximately 20 min. A thin copper foil (0.3 mm) was used as filter. Phoenix datos x software was used for the 3D image reconstruction and data were analysed with the software ImageJ [27]. The thresholding was performed automatically using an IsoData algorithm. Pores with a volume smaller than 9 voxels were filtered out and therefore, the smallest pore equivalent diameter that can be detected was about 7,7 μm. The reconstructed 3D samples were used to analyse internal defects and surface roughness as illustrated in Figure 2. The calculation of the relative density of the parts was performed from the 3D images, by computing the ratio between the volume of the sample (without pores) and the total volume of pores.

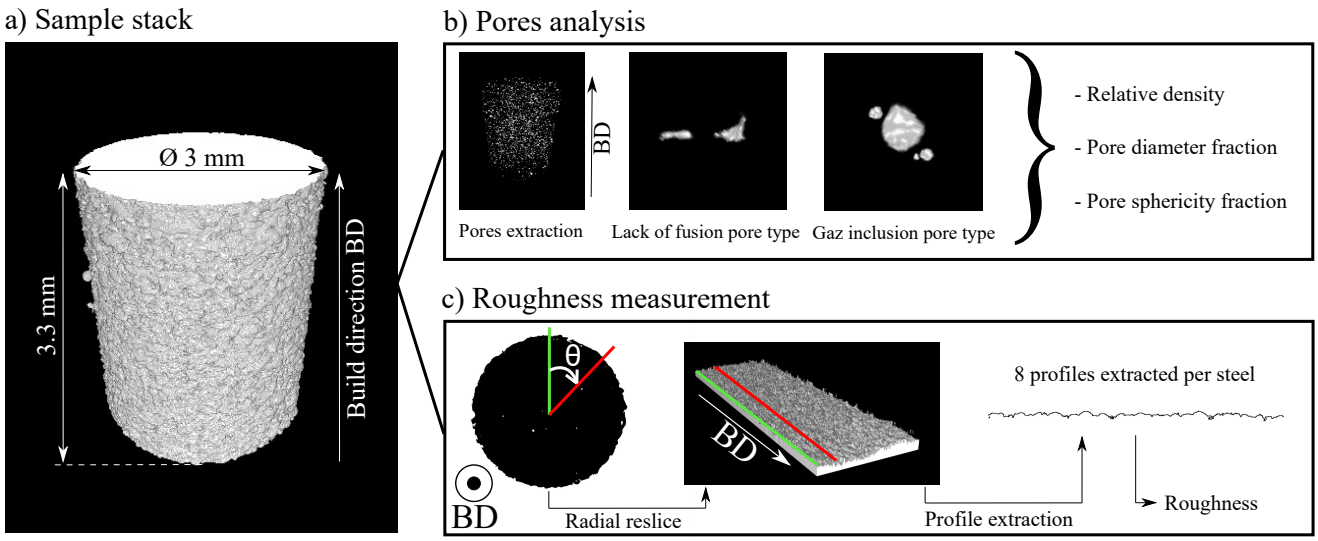

Figure 2: X-ray tomography analysis; a) 3D sample reconstruction in ImageJ; b) Relative density, pore diameter fraction, pore sphericity; c) Roughness analysis based on a method developed in [28][29]

In order to characterize the surface quality of the as-built samples, lateral surface profiles were extracted from the X-ray scans as shown in Figure 2c) using a method developed in [28][29]. The roughness is characterized with the R_a and R_t indicators defined by the equations :

$$R_a = \frac{1}{N}\sum_{i=0}^{N} |f_n|$$

$$R_t = max(f_n) + |min(f_n)|$$

where f_n is the height of peaks or depths obtained from the profiles extracted from the reconstructed 3D samples at N positions along the extracted profiles. As f_n values were obtained from to X-ray scans, it was possible to observe thin defects and cavities impossible to detect with profilometer diamond stylus or confocal microscope.

The sphericity of the pores was calculated by carrying out the ratio between the real surface of the pore and the surface of a sphere of volume equivalent to that of the pore. Sphericity values range between 0 and 1, the latter being the sphericity of a perfect spherical pore.

Pore projection was done using minimum intensity projection in ImageJ. Minimum Intensity projection creates a 2D (X,Y) image where each pixel has the minimum value over all images in the Z (build direction) stacks at the (X,Y) position of the pixel as explained in [30]. In our case, pores had the minimum values after thresholding, and projections were made along the construction axis. Therefore, pores at different heights in the sample can be seen in a 2D view.

2.5. Characterization of the crystallographic structure

A D8 Advance Bruker AXS diffractometer was used to perform X-ray diffraction (XRD) at 4 kV and 40 mA with CuK_α radiation (1.54 Å). Scans were acquired in a $\theta - \theta$ configuration from 30° to 130° (2θ) with a step size of 0.05° and a step time of 1 s. Austenite quantification was performed using TOPAS software.

3. Results and discussion

3.1. Cracks, pores and surface roughness

The presence of cracks, pores and relatively large surface roughness is an inherent problem encountered in LPBFed parts. They have detrimental consequences on the fatigue behaviour of the parts because they can lead to stress concentration and consequently to failure [11][31][32][33].

Cracks are observable in martensitic non-stainless steels Charpy specimens (42CD4, H11, H13, PM2012) as illustrated Figure 3. The cracks are mainly located at the base of the samples, i.e. close to the fabrication plate, this phenomenon has already been observed in [26][34]. It was shown in [35] that the maximum stresses are found at the connection between the specimen and the fabrication plate. The propagation of a crack in an H13 specimen is visible in the Figure 4. The crack appears to start at a surface defect. It propagates initially horizontally at the interface between the fusion layers, resulting from delamination. It then changes direction probably due to the state of stress. Other steels did not crack, even martensitic stainless steels, which contain as much carbon as martensitic non-stainless steels. No cracks were observed in the cylinders used for tomography, except in the PM2012 cylinders as illustrated Figure 5. The absence of cracks in the cylinders is probably related to the small size of these parts compared to the Charpy specimens and therefore to their lower stress concentration.

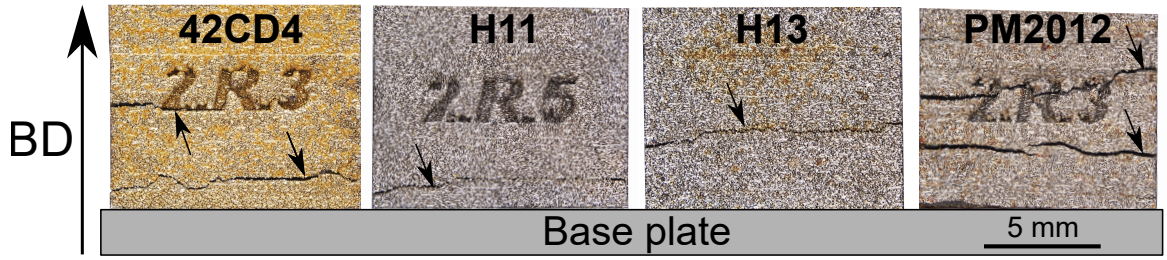

Figure 3: Cracks on martensitic non-stainless Charpy specimens. Cracks are mainly located at the base of the specimens where the residual stresses are the highest.

Figure 4: A crack in an H13 sample observed after a chemical etching with Fry's reagent. Delamination is visible in the red circle.

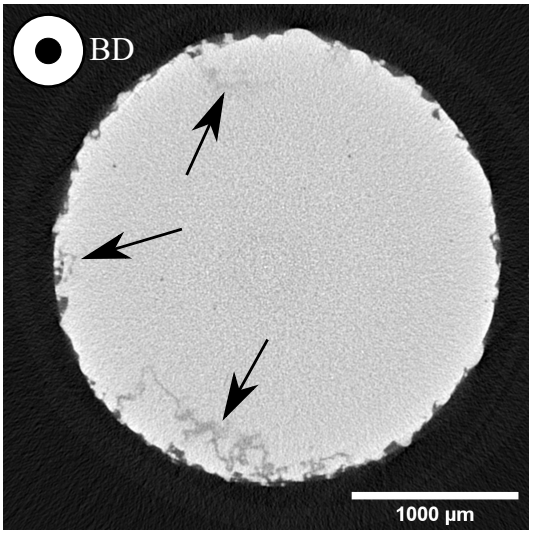

Figure 5: Cracks inside PM2012 cylinder used for X-ray tomography. Only PM2012 cylinders exhibit cracks.

Concerning internal defects, two different types of pores can be observed: spherical pores, resulting from the formation of keyholes or gas inclusions in powders; and non-spherical pores, resulting from a lack-of-fusion as shown in Figure 2.b. and Figure 6.

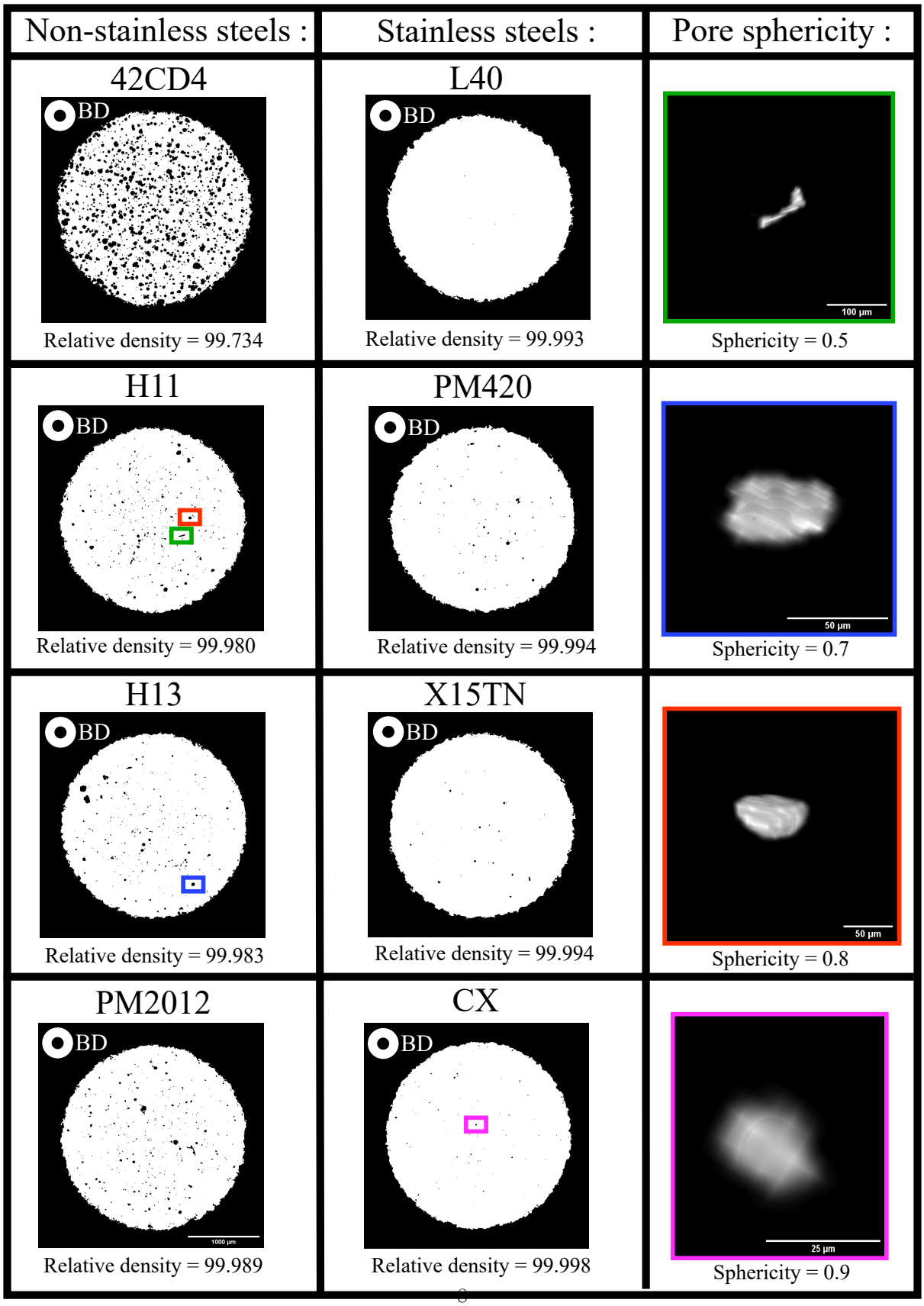

Figure 6: Pore projection following the manufacturing axis showing the part volume, and pore shape. Some pores may overlap due to projection creating an apparent irregular shape.

Table 3 shows that all the printed steels are nearly fully dense. Relative densities are all higher than 99.8% except for 42CD4 (99.7%). Stainless steels are slightly denser than the non-stainless steels, this may result from the different sets of parameters used. It was found that the relative density does not vary along the construction axis for all steels. For instance, Figure 7 shows the relative density of a 42CD4 sample along the construction axis Z.

Table 3: Porosity, pore size and roughness determined by X-Ray tomography. Internal defects and roughness are homogeneous between the steels. Only 42CD4 presents a lower relative density than the other steels.

Steel types	**Martensitic stainless steels**		**Martensitic non-stainless steels**				**Maraging stainless steels**	
Steel names	**PM420**	**X15TN**	**42CD4**	**AISI H11**	**AISI H13**	**PM2012**	**L40**	**CX**
Relative density (%)	99.994	99.994	99.734	99.980	99.983	99.990	99.993	99.998
Sphericity median value	0.70	0.72	0.82	0.77	0.69	0.77	0.67	0.76
Pore diameter median value (μm)	29	27	39	25	33	24	30	18
R_a (μm)	15.1	14.1	14.1	13.7	14.5	14.2	13.1	12.4
R_t (μm)	121.1	110.4	116.3	116.4	129.9	116.3	112.7	96.3

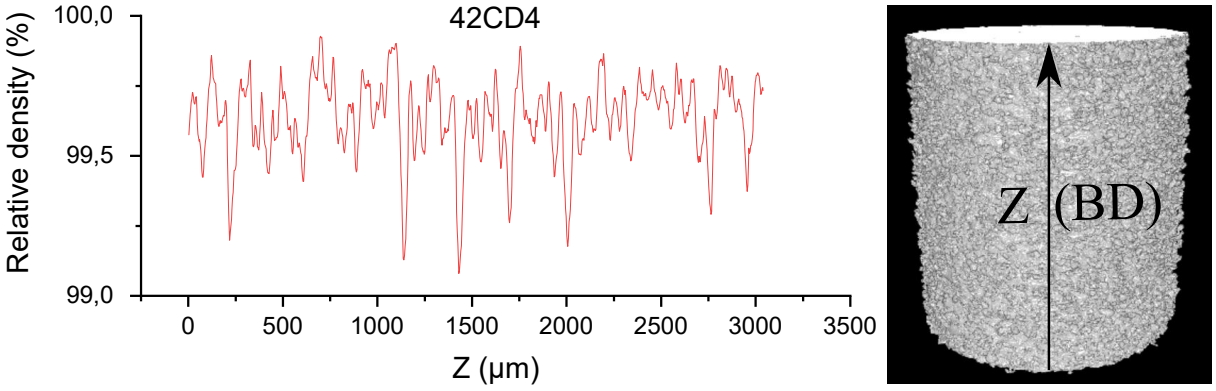

Figure 7: Relative density as a function of height Z in 42CD4

However, the amount of pores increases close to the surface in all samples. This can be observed when the pore projection is done without showing the volume of the part as illustrated Figure 8.a) for PM420. Such pores are not visible on Figure 6 as their position near the surface makes them less visible because of the black background.

Such pores might be caused by the acceleration and deceleration of the laser beam at the edges of the samples resulting in locally higher energy densities and therefore in pore formations as illustrated Figure 8.b). In our case, this hypothesis is unlikely as the EOS M270 machine used for printing has a "sky-writing" mode which allows the mirrors to reach the scanning speed before switching on the laser beam [36][37][38][39]. A second hypothesis is that at the beginning and at the end of the printing of a cylindrical layer the length of the weld beads is shorter, and therefore the beads have less time to cool down between each laser run than at the central part of the layer as shown Figure 8.c). Since each layer is printed with an angle of 67° with the previous layer, the presence of pores is detectable all around the sample. A concentric scanning strategy

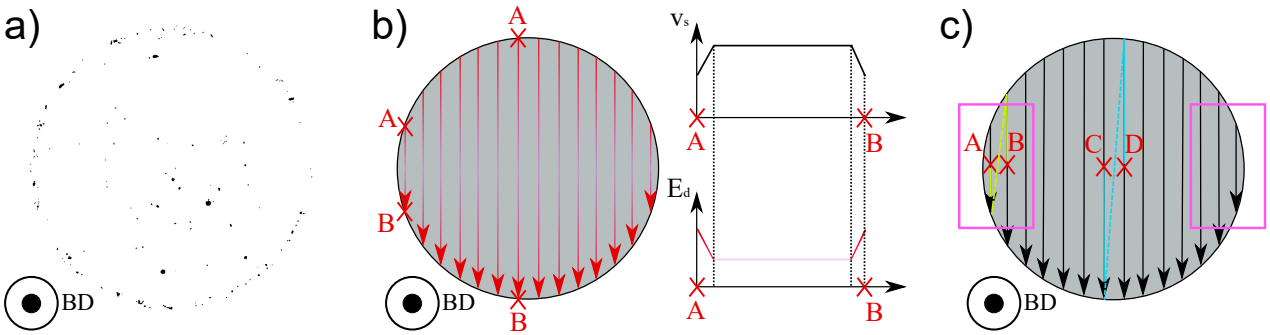

Figure 8: Projection showing the more important amount of pores close to the surface and hypotheses to explain this phenomenon. a) Projection of the pores in PM420 within the volume of the sample. The amount of pores increases close to the surface of the samples. Same observations were made in all the samples ; b) First hypothesis on the higher presence of pores at the edge of the samples. The grey circle represents the layer of the sample being printed and the arrows represent the weld beads. If the laser accelerates at the beginning of the weld bead formation to reach the required scanning speed and decelerates at the end, the energy density will locally be more important. This higher energy density may be responsible for the formation of pores at the edge of the specimens by keyholing. c) Second hypothesis on the greater presence of pores at the edge of the samples. The grey circle represents the layer of the sample being printed and the arrows represent the weld beads. The distance the laser has to travel from point A to point B (yellow lines) is smaller than from point C to point D (blue lines). This means that the material has less time to cool down when the laser fuses the bead from point B than when it fuses the bead from point D. Also, the closer the laser is to an edge, the slower the bead will cool down since the thermal conductivity of the powder bed is lower than that of the printed part. For these reasons, as the material gets warmer, it is possible that pores will appear in the areas highlighted in pink by keyholing. Since each layer is printed with an angle of 67° from the previous one, pores are observable over the whole height of the sample.

could be tried to avoid a localized higher energy density.

Median values are presented in Table 3 for all steels. They range between 0.67 and 0.82 which means that more than half of the pore volume is composed of quasi-spherical pores. A typical illustration of the pores 3D shape are given in Figure 6. The pore diameter median values given in Table 3 show that the median diameter sizes for all steels range between 18 and 39 μm. So, globally, pores are very similar in size and shape for all steels.

Concerning surface roughness, melting parameters can lead to roughness by causing lack of powder fusion and balling effect [11].

The results of roughness measurements are shown in Table 3. Overall, both R_a and R_t values remain constant for the different materials ($R_a \sim 14$ μm, $R_t \sim 120$ μm). Those values are similar to the ones reported by [11][40] for 316L and AISI H13 materials.

Consequently, the tomographic analysis shows that the different steels are comparable in terms of pore characteristics and roughness, regardless of the melting parameters used to print them, except for 42CD4 that presents a higher porosity.

3.2. Microstructure analysis

XRD analyses were performed on all steels, patterns are given in Figure 9.a) and the amount of austenite in each steel is given in Figure 9.b).

Retained austenite is due to incomplete martensitic transformation, i.e. when the martensite finish temperature M_f is not reached because M_f and M_s (the martensite start temperature) are low. These temperatures depend on the concentrations of the alloying elements and can be estimated using empirical equations [41][42][43]. It has been shown in [44] that the Steven & Haynes equation [42] :

$$M_s = 561 - 474C - 33Mn - 17Ni - 17Cr - 21Mo$$

and Andrews equation [43] :

$$M_s = 539 - 423C - 30,4Mn - 17,7Ni - 12,1Cr - 7,5Mo$$

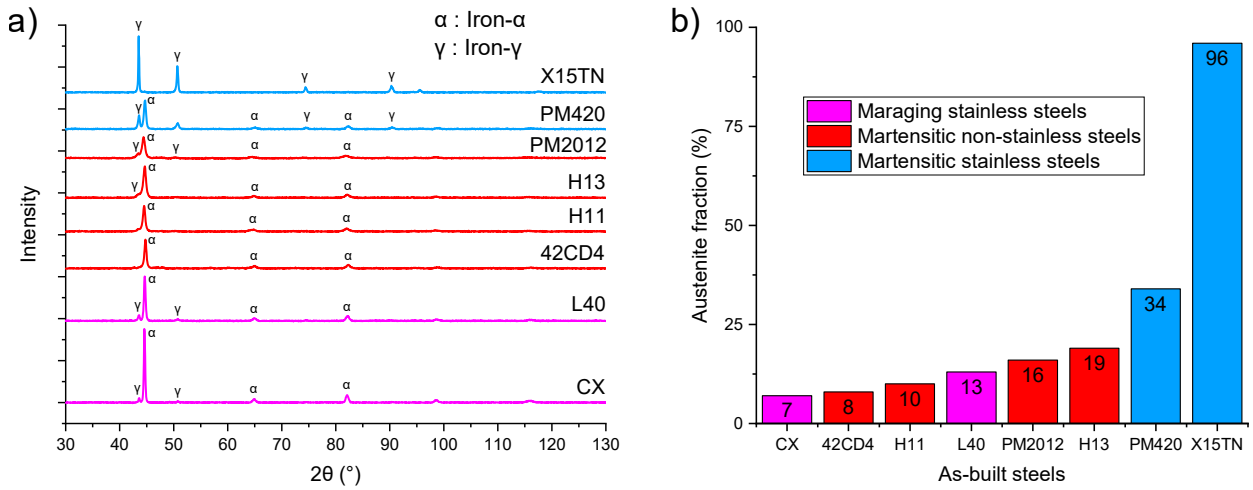

Figure 9: XRD analysis : a) XRD patterns of the as-built steels. All steels present iron-α and iron-γ peaks, except the X15TN which only shows iron-γ peaks, meaning is mainly composed of austenite after melting ; b) Austenite fraction from the XRD pattern. Martensitic stainless steels contained an important amount of austenite in the as-built state.

are particularly efficient for estimating the M_s temperatures of low- and high-alloy steels. However, the Andrews equation overestimates the M_s of high Cr steels while the Steven & Haynes equation underestimates the M_s of high Mo steels [44]. These equations highlight the impact of the elements C, Mn, Ni, Cr and Mo on the reduction of M_s temperature.

The M_s temperatures calculated for the eight steels are given in the Table 4. The percentage of austenite detected in relation to the M_s temperature is shown in the Figure 10. X15TN is the steel with the lowest M_s temperature and it is also the steel with the highest austenite content after melting. This is due to its higher concentration of alloying elements. 42CD4, H11, H13 and L40 have the highest M_s temperature and also the lowest austenite content. PM420, PM2012 and CX steels have similar M_s temperatures. The higher concentration of austenite in PM420 is probably related to a reversion of austenite, which is caused by the tempering of the lower layers during printing of the upper layers. This phenomenon was highlighted in AISI 420 in [45] and results from a local increase in carbon content at either retained austenite grains interfaces or at interfaces between martensite and austenite [46]. The lower fraction of austenite in PM2012 is probably related to the lower energy density used for printing, resulting in less tempering of the lower layers and therefore less reversion. For CX, no reversion could take place since it does not contain carbon.

It is possible that the crack-free printing of high carbon martensitic stainless steels is related to this large amount of austenite after LPBF printing. Austenite is much softer than martensite, can be highly deformed, and is therefore less prone to cracking. Stainless maraging steels have a lower quantity of austenite after melting, probably because of their lower carbon content which is a strong stabilizing element for austenite.

Table 4: M_s temperatures of the steels estimated using Stevens & Haynes and Andrews empirical formulas

Steel types	**Martensitic stainless steels**		**Martensitic non-stainless steels**				**Maraging stainless steels**	
Steel names	**PM420**	**X15TN**	**42CD4**	**AISI H11**	**AISI H13**	**PM2012**	**L40**	**CX**
M_s (°C) Steven & Haynes	151	51	313	243	272	157	240	153
M_s (°C) Andrews	215	150	322	285	311	213	297	204

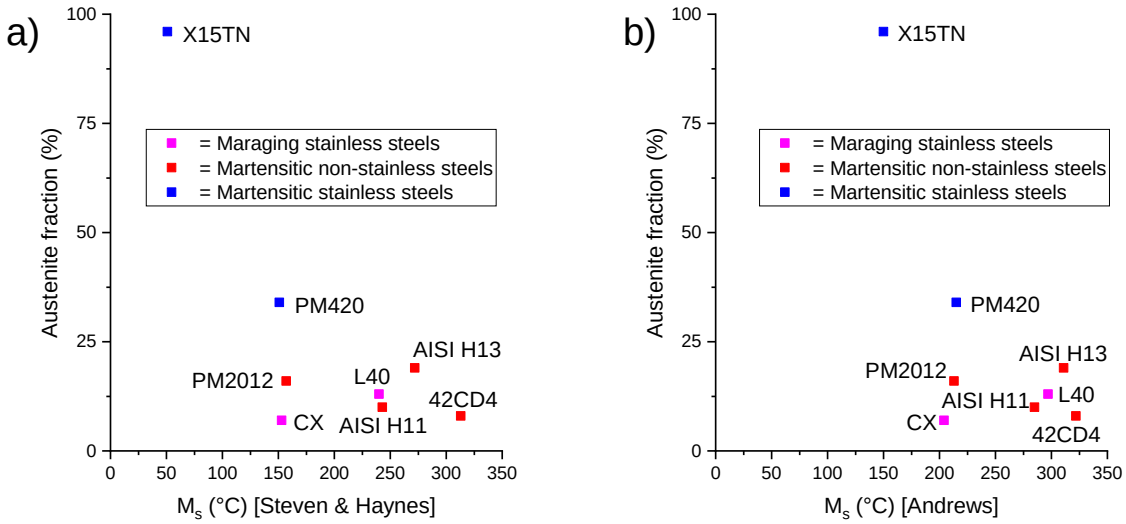

Figure 10: Austenite fraction detected by XRD depending on M_s temperature : a) According to Steven & Haynes [42] ; b) According to Andrews [43]

3.3. Mechanical properties

Hardness and Charpy impact tests show a significant heterogeneity between the different kinds of steels (Figure 11). As could be expected, martensitic non-stainless steels and martensitic stainless steels are the hardest ($\sim$ 53 HRC) and most brittle ($\sim$ 15 J/cm^2), and maraging the softest ($\sim$ 40 HRC) and most ductile ($\sim$ 100 J/cm^2). This is likely to be related to the lower carbon content in the maraging steels than in the martensitic steels (Table 1). However the carbon content is not the only factor influencing the mechanical properties of LPBFed parts. Figure 12.a) shows that 42CD4 and X15TN steels have lower hardness than H11 and H13 steels, although their carbon content is similar. 42CD4 is probably softer due to its lower relative density compared to other steels, while X15TN is probably softer due to its high austenite content after melting (Figure 12.b)).

Surface roughness, presence of pores and cracks, loss of alloying elements and residual stresses are inherent defects in AM affecting the mechanical properties of the fused parts [47]. It has been shown previously that internal defects and roughness are similar for all steels. Concerning the residual stresses, X-ray diffraction measurements in accordance with the NF EN 15305 standard have been carried out but the results were very scattered.

Maraging steels are the softest and most ductile because they are mainly composed of soft martensite i.e. a martensite with relatively low carbon content.

The X15TN is surprisingly soft for a steel with high carbon content (Figure 12.a)). It is also slightly less brittle than martensitic non-stainless steels. This is probably because it is mainly composed of austenite after fusion (Figure 12.b)).

Regarding the PM420, its hardness is comparable to the martensitic non-stainless steels and it has a better ductility than the X15TN and the martensitic non-stainless steels. This is possibly due to the presence of austenite in the PM420 (34%) after melting, higher than in the AISI H13 (19%).

Figure 13 shows that maraging (represented by CX) and martensitic (represented by PM420) have different failure modes. A strong plastic deformation of the maraging before fracture is observed Figure 13a) with, on a microscopic scale, the formation of dimples as shown in Figure 13c), proving the ductile nature of the fractures. Concerning the fracture surface of martensitic steels, the plastic deformation of the specimens before fracture is negligible (Figure 13b)) and no ductile dimples are detected (Figure 13d)), showing a brittle fracture. No defects could be identified as the initiator of the fracture.

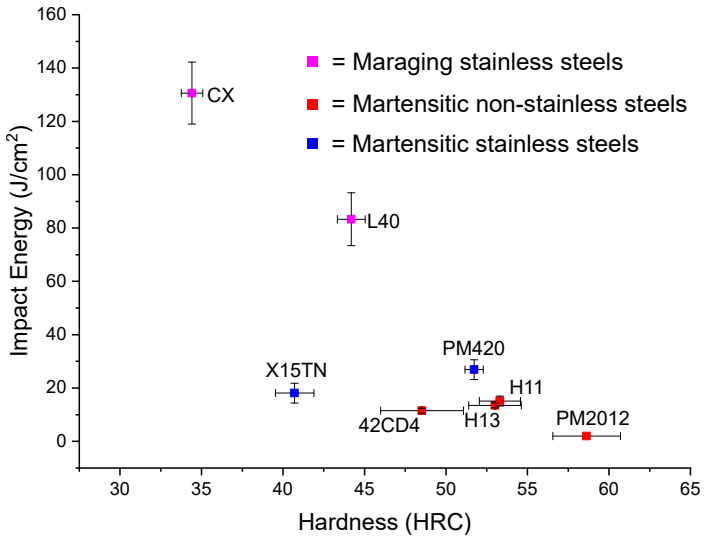

Figure 11: As-built hardness and impact energy. Martensitic non-stainless steels are the hardest and the more brittle materials. Martensitic stainless steels are softer and tougher than the martensitic non-stainless steels, this may be due to their higher content in austenite after melting. Maraging steels are soft and resilient after melting.

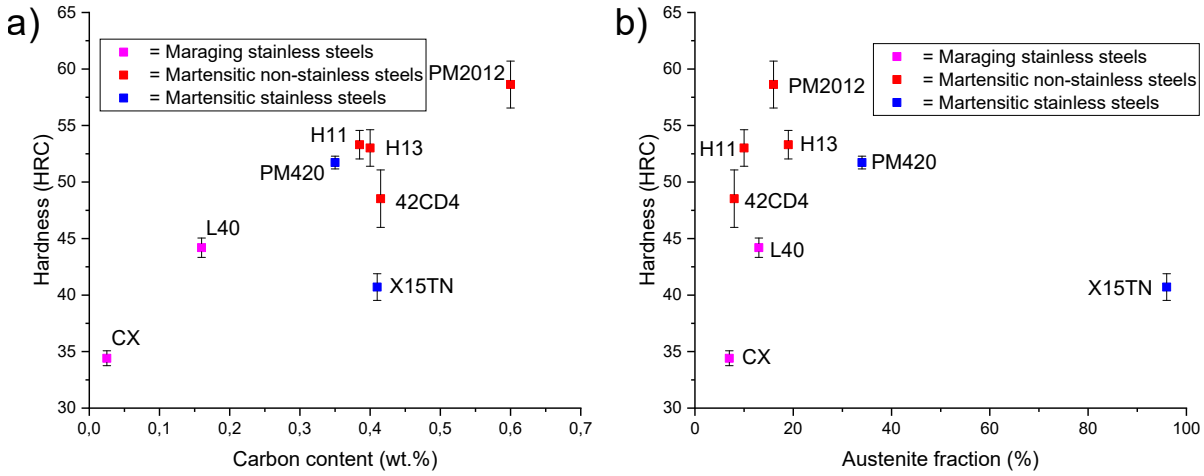

Figure 12: Hardness depending on a) carbon content and b) austenite fraction

4. Assessment of complex mold printing

After microstructural and mechanical characterization, the manufacturing of complex conformal cooling mold was assessed (Figure 14). This first attempt was performed using PM420 powder, this steel showed an excellent strength/ductility compromise.

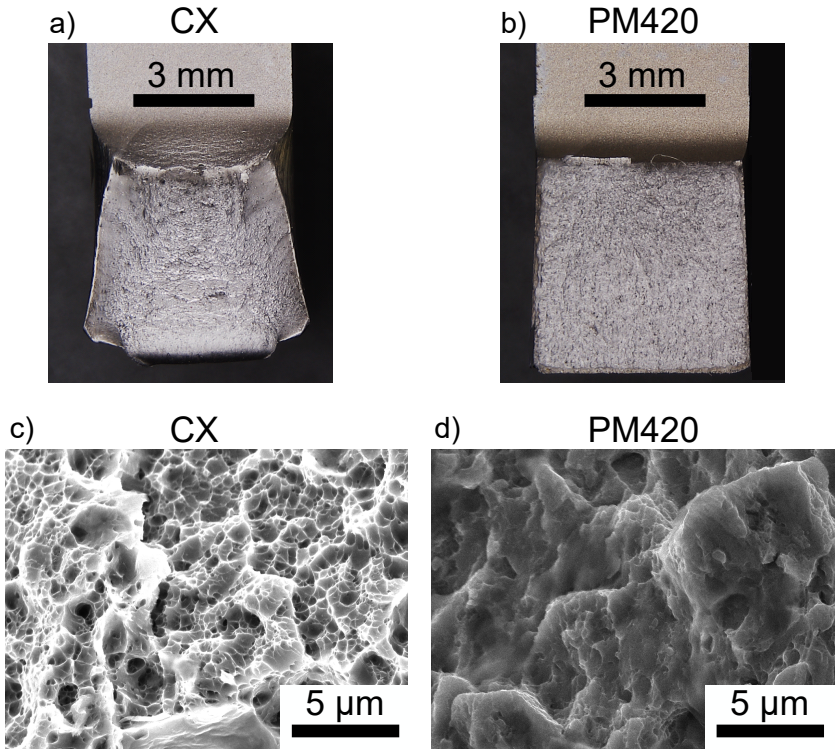

Figure 13: Fracture surfaces of CX and PM420 steels observed by optical (a-b) and SEM (c-d)

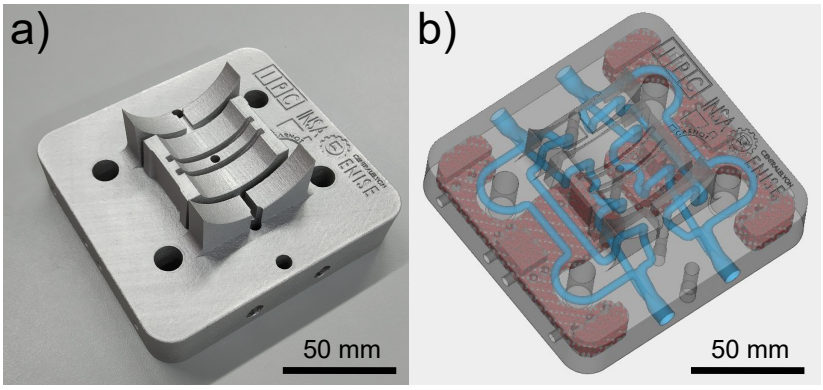

Figure 14: Examples of molds printed in PM420. The dimensions of the mold are 100x100x20 mm for the platform and 50x50x20 mm for the molding surface. b) highlights in red the lattice structure in the mold and in blue the cooling channels.

5. Conclusion

In this study, the printability of eight different steels was investigated through their mechanical properties, their defects, and their microstructure in the as-built state. The results show that:

- All martensitic non-stainless steels cracked during printing. The martensitic stainless steels did not crack even if they contain the same quantity of carbon than the martensitic non-stainless steels. This good printability of martensitic stainless steels may originate from a large amount of austenite, which can accept plastic deformation during printing.

- The melting parameters used in this study allow to obtain nearly fully dense parts. The internal defects are similar between the different steels except for 42CD4, which has a lower density than other steels.
- For all steels, relative density does not vary along the build direction but the amount of pores increases close to the surface.
- The median sizes of the pores observed are less than 50 μm. The median sphericities are between 0.67 and 0.82, indicating that more than half of the pore volume is composed of quasi-spherical pores.
- As maraging stainless steels are the softest and the less brittle steels because they form a relatively "soft" martensite after melting, they have the best printability.
- In spite of the very high density achieved, martensitic non-stainless steels have the lowest printability due to the high hardness of the martensite formed during printing.
- PM420 did not crack and has a good compromise between hardness and ductility. It is comparable in hardness to martensitic non-stainless steels and is more resilient than martensitic steels and X15TN, probably because of its high austenite content after melting (34%).
- X15TN did not crack neither, even though it contains as much carbon as martensitic non-stainless steels. This is probably because it is mainly composed of austenite after fusion (96%). It is softer than the other martensitic steels and it is slightly less brittle than martensitic non-stainless steels but is more brittle than PM420.
- PM420, X15TN, CX and L40 are possible alternatives to the 18Ni300 maraging steel to print molds by LPBF as they are printable, cobalt-free, and stainless steel.
- In order to determine whether the steels identified as potential alternatives to 18Ni300 can really be, they should be heat-treated. Indeed, maraging steels are designed to be aged and martensitic steels are generally tempered. A dedicated study on the effect of heat treatment on the properties of printed parts is on-going.

References

[1] S. Han, F. Salvatore, J. Rech, J. Bajolet, Abrasive flow machining (AFM) finishing of conformal cooling channels created by selective laser melting (SLM), Precision Engineering 64 (2020) 20–33. doi:10.1016/j.precisioneng.2020.03.006.
URL http://www.sciencedirect.com/science/article/pii/S0141635919306567

[2] A. Armillotta, R. Baraggi, S. Fasoli, SLM tooling for die casting with conformal cooling channels, The International Journal of Advanced Manufacturing Technology 71 (1) (2014) 573–583. doi:10.1007/s00170-013-5523-7.
URL https://doi.org/10.1007/s00170-013-5523-7

[3] M. Mazur, P. Brincat, M. Leary, M. Brandt, Numerical and experimental evaluation of a conformally cooled H13 steel injection mould manufactured with selective laser melting, The International Journal of Advanced Manufacturing Technology 93 (1-4) (2017) 881–900. doi:10.1007/s00170-017-0426-7.
URL http://link.springer.com/10.1007/s00170-017-0426-7

[4] K. Kempen, E. Yasa, L. Thijs, J. P. Kruth, J. Van Humbeeck, Microstructure and mechanical properties of Selective Laser Melted 18Ni-300 steel, Physics Procedia 12 (2011) 255–263. doi:10.1016/j.phpro.2011.03.033.
URL http://www.sciencedirect.com/science/article/pii/S187538921100112X

[5] N. Kang, W. Ma, L. Heraud, M. El Mansori, F. Li, M. Liu, H. Liao, Selective laser melting of tungsten carbide reinforced maraging steel composite, Additive Manufacturing 22 (2018) 104–110. doi:10.1016/j.addma.2018.04.031.
URL http://www.sciencedirect.com/science/article/pii/S2214860418302446

[6] L. M. S. Santos, L. P. Borrego, J. A. M. Ferreira, J. de Jesus, J. D. Costa, C. Capela, Effect of heat treatment on the fatigue crack growth behaviour in additive manufactured AISI 18Ni300 steel, Theoretical and Applied Fracture Mechanics 102 (2019) 10–15. doi:10.1016/j.tafmec.2019.04.005.
URL http://www.sciencedirect.com/science/article/pii/S0167844218305251

[7] J. Yan, Y. Zhou, R. Gu, X. Zhang, W.-M. Quach, M. Yan, A Comprehensive Study of Steel Powders (316L, H13, P20 and 18Ni300) for Their Selective Laser Melting Additive Manufacturing, Metals 9 (1) (2019) 86. doi:10.3390/met9010086.
URL https://www.mdpi.com/2075-4701/9/1/86

[8] G. Mohr, S. J. Altenburg, K. Hilgenberg, Effects of inter layer time and build height on resulting properties of 316L stainless steel processed by laser powder bed fusion, Additive Manufacturing 32 (2020) 101080. doi:10.1016/j.addma.2020.101080.
URL http://www.sciencedirect.com/science/article/pii/S2214860419311364

[9] Y. Sun, A. Moroz, K. Alrbaey, Sliding Wear Characteristics and Corrosion Behaviour of Selective Laser Melted 316L Stainless Steel, Journal of Materials Engineering and Performance 23 (2) (2014) 518–526. doi:10.1007/s11665-013-0784-8.
URL https://doi.org/10.1007/s11665-013-0784-8

[10] M. Mazur, M. Leary, M. McMillan, J. Elambasseril, M. Brandt, SLM additive manufacture of H13 tool steel with conformal cooling and structural lattices, Rapid Prototyping Journal 22 (3) (2016) 504–518. doi:10.1108/RPJ-06-2014-0075.
URL http://www.emeraldinsight.com/doi/10.1108/RPJ-06-2014-0075

[11] M. Narvan, K. S. Al-Rubaie, M. Elbestawi, Process-Structure-Property Relationships of AISI H13 Tool Steel Processed with Selective Laser Melting, Materials 12 (14) (2019) 2284. doi:10.3390/ma12142284.
URL https://www.mdpi.com/1996-1944/12/14/2284

[12] J. Damon, R. Koch, D. Kaiser, G. Graf, S. Dietrich, V. Schulze, Process development and impact of intrinsic heat treatment on the mechanical performance of selective laser melted AISI 4140, Additive Manufacturing 28 (2019) 275–284. doi:10.1016/j.addma.2019.05.012.
URL http://www.sciencedirect.com/science/article/pii/S2214860418309369

[13] R. Casati, M. Coduri, N. Lecis, C. Andrianopoli, M. Vedani, Microstructure and mechanical behavior of hot-work tool steels processed by Selective Laser Melting, Materials Characterization 137 (2018) 50–57. doi:10.1016/j.matchar.2018.01.015.
URL http://www.sciencedirect.com/science/article/pii/S1044580317332539

[14] M. Ackermann, J. Šafka, L. Voleský, J. Bobek, J. R. Kondapally, Impact Testing of H13 Tool Steel Processed with Use of Selective Laser Melting Technology, Materials Science Forum 919 (2018) 43–51. doi:10.4028/www.scientific.net/MSF.919.43.
URL https://www.scientific.net/MSF.919.43

[15] J. Džugan, K. Halmešová, M. Ackermann, M. Koukolíková, Z. Trojanová, Thermo-physical properties investigation in relation to deposition orientation for SLM deposited H13 steel, Thermochimica Acta 683 (2020) 178479. doi:10.1016/j.tca.2019.178479.
URL http://www.sciencedirect.com/science/article/pii/S0040603119307312

[16] T. Kurzynowski, W. Stopyra, K. Gruber, G. Ziółkowski, B. Kuźnicka, E. Chlebus, Effect of Scanning and Support Strategies on Relative Density of SLM-ed H13 Steel in Relation to Specimen Size, Materials 12 (2) (2019) 239. doi:10.3390/ma12020239.
URL https://www.mdpi.com/1996-1944/12/2/239

[17] P. Laakso, T. Riipinen, A. Laukkanen, T. Andersson, A. Jokinen, A. Revuelta, K. Ruusuvuori, Optimization and Simulation of SLM Process for High Density H13 Tool Steel Parts, Physics Procedia 83 (2016) 26–35. doi:10.1016/j.phpro.2016.08.004.
URL http://www.sciencedirect.com/science/article/pii/S1875389216301110

[18] W. Sha, A. Cerezo, G. D. W. Smith, Phase chemistry and precipitation reactions in maraging steels: Part II. Co-free T-300 steel, Metallurgical and Materials Transactions A 24 (6) (1993) 1233–1239. doi:10.1007/BF02668191.
URL https://doi.org/10.1007/BF02668191

[19] R. Lauwerys, D. Lison, Health risks associated with cobalt exposure — an overview, Science of The Total Environment 150 (1) (1994) 1–6. doi:10.1016/0048-9697(94)90125-2.
URL http://www.sciencedirect.com/science/article/pii/0048969794901252

[20] M. De Boeck, M. Kirsch-Volders, D. Lison, Cobalt and antimony: genotoxicity and carcinogenicity, Mutation Research/Fundamental and Molecular Mechanisms of Mutagenesis 533 (1) (2003) 135–152. doi:10.1016/j.mrfmmm.2003.07.012.
URL http://www.sciencedirect.com/science/article/pii/S0027510703002136

[21] C. D. Tuffile, H. Lemke, 3d printable hard ferrous metallic alloys for powder bed fusion (Aug. 2019).
URL https://patents.google.com/patent/US20190262944A1/en?assignee=formetrix&oq=formetrix

[22] M. Limousin, C. Colin, P. Bertrand, L. Van Belle, Heat Treatment Optimization of a High Nitrogen Stainless Steel Manufactured by Laser Beam Melting, in: Proc. of Word PM2016, Euro PM Published, Aachen, Germany, 2016.
URL https://search.proquest.com/openview/6030beb469d2635f47fb8379cd322cb4/1?pq-origsite=gscholar&cbl=596295

[23] N. Maillol, D. B. Mataix, A. Tommasi, T. Joffre, J. Bajolet, Impact of Exposure Parameters on Tooling Steel Properties and Performance, in: Proc. of Euro PM2018, Euro PM Published, Madrid, Spain, 2018.
URL https://works.bepress.com/bernhard-heiden/8/

[24] L. Van Belle, J.-C. Boyer, G. Vansteenkiste, Investigation of residual stresses induced during the selective laser melting process, Key Engineering Materials 554-557 (2013) (2013) 1828–2834. doi:10.4028/www.scientific.net/KEM.554-557.1828.
URL https://hal.archives-ouvertes.fr/hal-00824655

[25] J. L. Bartlett, X. Li, An overview of residual stresses in metal powder bed fusion, Additive Manufacturing 27 (2019) 131–149. doi:10.1016/j.addma.2019.02.020.
URL http://www.sciencedirect.com/science/article/pii/S221486041930051X

[26] M. F. Zaeh, G. Branner, Investigations on residual stresses and deformations in selective laser melting, Production Engineering 4 (1) (2010) 35–45. doi:10.1007/s11740-009-0192-y.
URL https://doi.org/10.1007/s11740-009-0192-y

[27] C. A. Schneider, W. S. Rasband, K. W. Eliceiri, NIH Image to ImageJ: 25 years of image analysis, Nature Methods 9 (7)

(2012) 671–675, number: 7 Publisher: Nature Publishing Group. doi:10.1038/nmeth.2089.
URL https://www.nature.com/articles/nmeth.2089

[28] T. Persenot, A. Burr, R. Dendievel, J.-Y. Buffière, E. Maire, J. Lachambre, G. Martin, Fatigue performances of chemically etched thin struts built by selective electron beam melting: Experiments and predictions, Materialia 9 (2020) 100589. doi:10.1016/j.mtla.2020.100589.
URL http://www.sciencedirect.com/science/article/pii/S2589152920300065

[29] T. Persenot, Fatigue of Ti-6Al-4V thin parts made by electron beam melting, Ph.D. thesis (2018).
URL http://www.theses.fr/235597090

[30] Stacks [ImageJ Documentation Wiki] (Apr. 2019).
URL https://imagejdocu.tudor.lu/gui/image/stacks

[31] R. Cunningham, S. P. Narra, C. Montgomery, J. Beuth, A. D. Rollett, Synchrotron-Based X-ray Microtomography Characterization of the Effect of Processing Variables on Porosity Formation in Laser Power-Bed Additive Manufacturing of Ti-6Al-4V, JOM 69 (3) (2017) 479–484. doi:10.1007/s11837-016-2234-1.
URL https://link.springer.com/article/10.1007/s11837-016-2234-1

[32] M. Speirs, B. Van Hooreweder, J. Van Humbeeck, J. P. Kruth, Fatigue behaviour of NiTi shape memory alloy scaffolds produced by SLM, a unit cell design comparison, Journal of the Mechanical Behavior of Biomedical Materials 70 (2017) 53–59. doi:10.1016/j.jmbbm.2017.01.016.
URL http://www.sciencedirect.com/science/article/pii/S1751616117300231

[33] O. Andreau, E. Pessard, I. Koutiri, J.-D. Penot, C. Dupuy, N. Saintier, P. Peyre, A competition between the contour and hatching zones on the high cycle fatigue behaviour of a 316L stainless steel: Analyzed using X-ray computed tomography, Materials Science and Engineering: A 757 (2019) 146–159. doi:10.1016/j.msea.2019.04.101.
URL http://www.sciencedirect.com/science/article/pii/S0921509319305763

[34] A. Royakkers, Selectief Laser Smelten van AISI M2 Snelstaal poeder, Master's thesis (2011).

[35] L. van Belle, G. Vansteenkiste, J.-C. Boyer, Comparisons of numerical modelling of the Selective Laser Melting (2012) 8.

[36] Y. Tian, D. Tomus, P. Rometsch, X. Wu, Influences of processing parameters on surface roughness of Hastelloy X produced by selective laser melting, Additive Manufacturing 13 (2017) 103–112. doi:10.1016/j.addma.2016.10.010.
URL https://www.sciencedirect.com/science/article/pii/S221486041630286X

[37] V.-P. Matilainen, H. Piili, A. Salminen, O. Nyrhilä, Preliminary Investigation of Keyhole Phenomena during Single Layer Fabrication in Laser Additive Manufacturing of Stainless Steel, Physics Procedia 78 (2015) 377–387. doi:10.1016/j.phpro.2015.11.052.
URL https://linkinghub.elsevier.com/retrieve/pii/S1875389215015424

[38] F. Calignano, G. Cattano, D. Manfredi, Manufacturing of thin wall structures in AlSi10Mg alloy by laser powder bed fusion through process parameters, Journal of Materials Processing Technology 255 (2018) 773–783. doi:10.1016/j.jmatprotec.2018.01.029.
URL https://www.sciencedirect.com/science/article/pii/S092401361830030X

[39] A. Mancisidor, F. Garciandia, M. S. Sebastian, P. Álvarez, J. Díaz, I. Unanue, Reduction of the Residual Porosity in Parts Manufactured by Selective Laser Melting Using Skywriting and High Focus Offset Strategies, Physics Procedia 83 (2016) 864–873. doi:10.1016/j.phpro.2016.08.090.
URL https://linkinghub.elsevier.com/retrieve/pii/S1875389216301973

[40] G. Strano, L. Hao, R. M. Everson, K. E. Evans, Surface roughness analysis, modelling and prediction in selective laser melting, Journal of Materials Processing Technology 213 (4) (2013) 589–597. doi:10.1016/j.jmatprotec.2012.11.011.
URL http://www.sciencedirect.com/science/article/pii/S0924013612003366

[41] A. Nehrenberg, The temperature range of martensite formation, Transactions AIME 167 (1946) 494–498.

[42] W. Steven, A. Haynes, The Temperature of Formation of Martensite and Bainite in Low-Alloy Steels, Journal of the Iron and Steel Institute 183 (8) (1956) 349–359.

[43] K. Andrews, Empirical formulae for the calculation of some transformation temperatures, Journal of the Iron and Steel Institute 203 (1965) 721–727.

[44] C. Y. Kung, J. J. Rayment, An examination of the validity of existing empirical formulae for the calculation of ms temperature, Metallurgical Transactions A 13 (2) (1982) 328–331. doi:10.1007/BF02643327.
URL https://doi.org/10.1007/BF02643327

[45] P. Krakhmalev, I. Yadroitsava, G. Fredriksson, I. Yadroitsev, In situ heat treatment in selective laser melted martensitic AISI 420 stainless steels, Materials & Design 87 (2015) 380–385. doi:10.1016/j.matdes.2015.08.045.
URL http://www.sciencedirect.com/science/article/pii/S026412751530294X

[46] L. Yuan, D. Ponge, J. Wittig, P. Choi, J. A. Jiménez, D. Raabe, Nanoscale austenite reversion through partitioning, segregation and kinetic freezing: Example of a ductile 2GPa Fe–Cr–C steel, Acta Materialia 60 (6) (2012) 2790–2804. doi:10.1016/j.actamat.2012.01.045.
URL http://www.sciencedirect.com/science/article/pii/S1359645412000833

[47] T. DebRoy, H. L. Wei, J. S. Zuback, T. Mukherjee, J. W. Elmer, J. O. Milewski, A. M. Beese, A. Wilson-Heid, A. De, W. Zhang, Additive manufacturing of metallic components – Process, structure and properties, Progress in Materials Science 92 (2018) 112–224. doi:10.1016/j.pmatsci.2017.10.001.
URL http://www.sciencedirect.com/science/article/pii/S0079642517301172